

# Mass-preserving Spatio-temporal adaptive PINN for Cahn-Hilliard equations with strong nonlinearity and singularity

Qiumei Huang<sup>a</sup>, Jiaxuan Ma<sup>a</sup>, Zhen Xu<sup>a,\*</sup>

<sup>a</sup>*School of Mathematics, Statistics and Mechanics, Beijing University of Technology, Beijing 100124, China*

---

## Abstract

As one kind important phase field equations, Cahn-Hilliard equations contain spatial high order derivatives, strong nonlinearities, and even singularities. When using the physics informed neural network (PINN) to simulate the long time evolution, it is necessary to decompose the time domain to capture the transition of solutions in different time. Moreover, the baseline PINN can't maintain the mass conservation property for the equations. We propose a mass-preserving spatio-temporal adaptive PINN. This method adaptively dividing the time domain according to the rate of energy decrease, and solves the Cahn-Hilliard equation in each time step using an independent neural network. To improve the prediction accuracy, spatial adaptive sampling is employed in the subdomain to select points with large residual value and add them to the training samples. Additionally, a mass constraint is added to the loss function to compensate the mass degradation problem of the PINN method in solving the Cahn-Hilliard equations. The mass-preserving spatio-temporal adaptive PINN is employed to solve a series of numerical examples. These include the Cahn-Hilliard equations with different bulk potentials, the three dimensional Cahn-Hilliard equation with singularities, and the set of Cahn-Hilliard equations. The numerical results demonstrate the effectiveness of the proposed algorithm.

*Keywords:* Cahn-Hilliard equations, Singularity, PINN, Mass constraint, Spatio-temporal adaptive sampling,

---

\*Corresponding author

*Email addresses:* qmhuang@bjut.edu.cn (Qiumei Huang),  
majiaxuan@emails.bjut.edu.cn (Jiaxuan Ma), xuzhenmath@bjut.edu.cn (Zhen Xu)

## 1. Introduction

The phase field model is widely applied to a variety of problems in materials science and life science. It utilizes the order parameter  $u$  to capture the diffusive interface between two phases. One of the classical equations of the phase field model is the Cahn-Hilliard equation proposed by Cahn and Hilliard[1, 2], which is used to simulate phase separation phenomena in binary metal mixtures. It is extended to simulate the motion of free interfaces during phase transitions. A variety of numerical methods related to time discretisation have been proposed for the phase field equations, such as convex splitting schemes[3–7], stabilized schemes[8–11], Invariant Energy Quadraticization (IEQ) method and its variants[12–14], Scalar Auxiliary Variable (SAV) and its variants[15–19], exponential time differencing(ETD) schemes [20, 21] and so on. These efficient and energy stable solutions have enjoyed remarkable success. However they also encounter certain difficulties when the energy of the phase field model is extremely complicated, where the equation contains singularities or complex boundary conditions. Specifically, the curse of dimensionality has always been another challenge for traditional numerical methods. Deep learning has the potential to solve high dimensional problems, so it has attracted the attention of researchers.

With the improvement of computational resources and the iteration of algorithms, deep learning has been widely utilized in various fields. Especially notable is the fact that some researchers have applied it to solve PDEs [22, 23]. When solving PDEs based solely on data-driven method, the lack of available data may leads to insufficient accuracy. Therefore, researchers consider introducing physical prior information to construct new deep learning based PDEs solvers. Karniadakis et al.[24] proposed physics informed neural networks (PINNs) to solve the forward and inverse problems, which encode the underlying physical laws into the loss function of the neural network to guide the training process. PINN transforms the problem of solving differential equations into an optimization problem, with the help of automatic differentiation not required to generate the grid. Thus, the algorithm has the potential to solve high-dimensional problems.

Although PINN has solved a number of PDEs, its computational efficiency and accuracy are limited when applied to complex problems such as the phase field equations. This is due to the highly nonlinearity and even singularity in the energy of phase field equations, as well as the stiffness caused by a small interface width. In particular, computing the high order derivatives of the Cahn-Hilliard equation in space is also challenging. Therefore, extensive research is dedicated to enhancing the adaptability and accuracy of PINN for various problems[25–27]. Specifically, since the distribution of sampling points affects the training result, researchers have proposed various effective sampling strategies, including DAS-PINN[28], FI-PINN[29], ACSM[30], RAD[31] and others. The most representative improvement

of the sampling strategy is the residual-based adaptive refinement (RAR) method proposed by Lu and Karniadakis et al.[32], which strengthens the training results by adding residuals with large residuals of the corresponding equations. Wight and Zhao[33] proposed a similar adaptive sampling method in space. Regarding the treatment of the time domain, Wight and Zhao[33] proposed an adaptive sampling method in time for the phase field equations to divide the time domain into small regions, which improves the accuracy of PINN in solving the phase field equations. Similarly, PPINN[34] decomposed a long time problem into several independent short time problems to be processed in parallel. As the weights of different terms in the loss function affect the training results, we can develop some strategies to adjust them. Researchers have introduced a range of adaptive and non-adaptive adjustment strategies[33, 35, 36]. Additionally, considering the conservation of physical quantities such as mass, energy, and momentum in certain equations, Lin et al.[37] developed a two-stage PINN method that incorporates conservation constraints into the loss function of PINN. This ensures that the solution preserves the original physical properties.

In this work, we propose the spatio-temporal adaptive PINN for the Cahn-Hilliard equations. We convert the fourth-order equation into a system of second order equations to reduce computational costs. A mass constraint is added to the loss function of PINN to ensure the mass conservation of predicted solutions. Based on the characteristics of the phase field equations evolving with time, we simulate them by dividing the time domain. The length and number of time subdomains are adjusted according to the energy evolution. Within each subdomain, the adaptive sampling in space is employed to enhance training effectiveness. The numerical results indicate that, compared to the results obtained with uniform time domain division as in [33], the absolute errors of predicted solutions for the Cahn-Hilliard equation with Ginzburg-Landau potential have significantly decreased. Simultaneously, we solve Cahn-Hilliard equation with Flory-Huggins potential with high singularity by adding a mapping to the network outputs. Furthermore, these solutions are able to maintain the property of mass conservation. At the end, we show some simulations performed with the spatio-temporal adaptive PINN to demonstrate its effectiveness for confined binary blended polymers model, which is a complex system of 2D phase field equations.

The rest of this article is organized as follows. In Section 2, we provide a brief overview of the architecture of the baseline PINN method, followed by an introduction to relevant improvement methods and strategies. Finally, we present the spatio-temporal adaptive PINN for high order phase field equations with mass conservation. In Section 3, we presented several numerical experiments to demonstrate the accuracy and efficiency of our method, followed by some simulations of three dimensional Cahn-Hilliard equation with Flory-Huggins potential and bi-

nary blended polymers model. At the end we give some conclusions in Section 4.

## 2. Methodology

In this section, we first briefly review PINN. Then we introduce the improvement of baseline PINN, including the sampling method and the setting of loss functions. Finally, we propose a spatio-temporal adaptive PINN method for high order phase field equations with mass conservation.

### 2.1. Review of physics informed neural networks

Consider the following general form of PDE:

$$\begin{aligned} u_t + \mathcal{N}[u] &= 0, & \mathbf{x} \in \Omega, & \quad t \in [0, T], \\ u(\mathbf{x}, 0) &= u_0(\mathbf{x}), & \mathbf{x} \in \Omega, \\ \mathcal{B}[u] &= 0, & \mathbf{x} \in \partial\Omega. \end{aligned} \tag{1}$$

Here,  $\Omega \subset \mathbb{R}^d$  is a bonded domain and  $\partial\Omega$  represents the boundary.  $\mathbf{x}$  and  $t$  are the space and time coordinates respectively,  $u$  is the solution of Equation (1).  $\mathcal{N}[\cdot]$  represents a linear or nonlinear differential operator related to the solution  $u$ , and  $\mathcal{B}[\cdot]$  is boundary operator, including periodic, Dirichlet, Neuman conditions, etc.

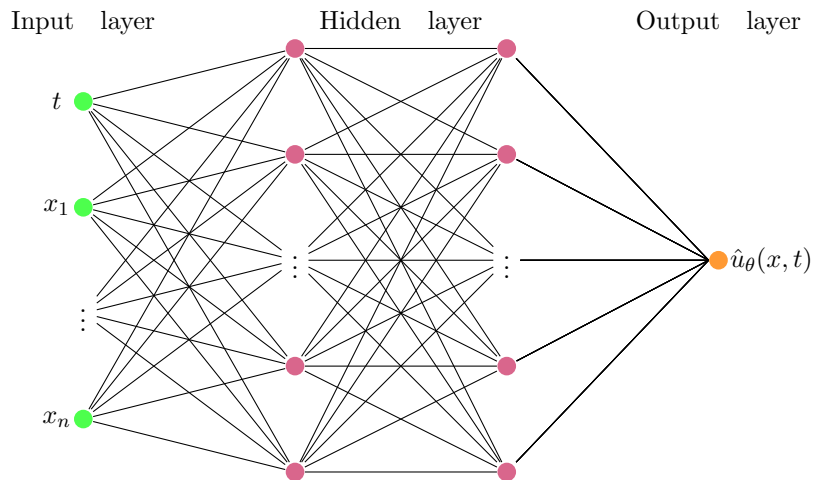


**Fig. 1.** Fully connected neural network

The main idea of PINN is to use the deep neural network  $\hat{u}_\theta(\mathbf{x}, t)$  as Fig. 1 with parameters  $\theta$  to approximate the real PDEs solution  $u(\mathbf{x}, t)$ . We consider the

feedforward fully connected neural network  $N_L(\mathbf{x})$  with  $L - 1$  hidden layers and  $n$  neurons per layer. The neural network is defined as follows:

$$\begin{aligned} \text{input layer : } & N_0(\mathbf{x}) = \mathbf{x}, \\ \text{hidden layer : } & N_i(\mathbf{x}) = \sigma(\mathbf{W}_i N_{i-1}(\mathbf{x}) + \mathbf{b}_i), \quad i = 1, \dots, L - 1, \\ \text{output layer : } & N_L(\mathbf{x}) = \mathbf{W}_L N_{L-1}(\mathbf{x}) + \mathbf{b}_L, \end{aligned} \quad (2)$$

where  $\sigma$  is the nonlinear activation function.  $\mathbf{W}_i$  and  $\mathbf{b}_i$  represent the weights and biases at  $i$ -th layer.  $\theta = \{\mathbf{W}_i, \mathbf{b}_i\}_{i=1}^L$  represents the trainable parameters of the neural network.

The loss function is to measure the difference between the output of the neural network and the expected output. In PINN, the gap between prediction solution and real solution is measured by the following loss function:

$$\mathcal{L}(\theta) = \lambda_u \mathcal{L}_u(\theta) + \lambda_b \mathcal{L}_b(\theta) + \lambda_r \mathcal{L}_r(\theta). \quad (3)$$

where,

$$\begin{aligned} \mathcal{L}_u(\theta) &= \frac{1}{N_u} \sum_{i=1}^{N_u} |\hat{u}_\theta(\mathbf{x}_u^i, t_u^i) - u_0(\mathbf{x}_u^i)|^2, \\ \mathcal{L}_b(\theta) &= \frac{1}{N_b} \sum_{i=1}^{N_b} |\mathcal{B}(\hat{u}_\theta(\mathbf{x}_b^i, t_b^i))|^2, \\ \mathcal{L}_r(\theta) &= \frac{1}{N_r} \sum_{i=1}^{N_r} \left| \frac{\partial \hat{u}_\theta}{\partial t}(\mathbf{x}_r^i, t_r^i) + N(\hat{u}_\theta(\mathbf{x}_r^i, t_r^i)) \right|^2. \end{aligned} \quad (4)$$

Here,  $\{\mathbf{x}_u^i, t_u^i\}_{i=1}^{N_u}$  and  $\{\mathbf{x}_b^i, t_b^i\}_{i=1}^{N_b}$  denote the initial points and boundary points, respectively. Moreover,  $\{\mathbf{x}_r^i, t_r^i\}_{i=1}^{N_r}$  is the set of residual points sampled from  $\Omega \times [0, T]$  by random sampling methods such as Latin hypercube sampling (LHS). The loss function (3) is a basic form, and we may introduce additional loss terms based on the specific case. The derivatives in the loss function are calculated through the automatic differentiation technique of the neural network[24], which avoids the complex discrete format of the derivatives in traditional numerical methods. The weight  $\lambda$  is a penalty factor to balance the various losses in the loss function. We can adjust the weights of different loss terms to obtain the best training result.

PINN transforms the problem of solving PDEs into a neural network optimization problem. The goal of training PINN is to find the optimal parameters  $\theta^*$  that minimizes the loss function, and this process is implemented using optimization algorithms such as stochastic gradient descent[38], Adam[39] and L-BFGS[40] etc. The numerical experiments in this paper are conducted by initially training with the Adam optimizer, followed by fine-tuning using the L-BFGS optimizer.

## 2.2. Improved methods for PINN

Baseline PINN can solve partial differential equations with smooth solutions, but is inadequate for solving equations with sharp interfaces and for long-time simulation of time-dependent partial differential equations. More importantly, it cannot perfectly preserve the physical properties of the equation such as conservation of mass. Next we present some improvements for PINN.

### 2.2.1. Adaptive Sampling in Space and Time

PINN can be regarded as a kind of semi-supervised learning. The simulation of the initial and boundary conditions belongs to supervised learning because their inputs have the corresponding data labels. The unsupervised learning part of PINN is the PDE residual, which are calculated by the residual points, as follows:

$$\mathcal{L}_r(\theta) = \frac{1}{N_r} \sum_{i=1}^{N_r} \left| \frac{\partial \hat{u}_\theta}{\partial t}(\mathbf{x}_r^i, t_r^i) + N(\hat{u}_\theta(\mathbf{x}_r^i, t_r^i)) \right|^2. \quad (5)$$

Since the PDE residual loss is evaluated on discrete residual points, the location and distribution of these residual points are critical to the performance of PINN. In [31], researchers summarize three types of strategies for selecting residual points in training: fixed residual points, uniform points with resampling, nonuniform adaptive sampling.

Here, fixed residual points means that a set of residual points is selected randomly at the beginning and the set of points is not changed during the whole training process. Uniform points with resampling first randomly selects a set of residual points to train PINN, and after a certain number of iteration steps, a new set of residual points is randomly sampled to replace the initial one. These two methods are generally effective for PDEs with smooth solutions, while not effective for phase field equations. This is because the solutions of phase field equations have moving interfaces in space, and the errors occur mainly at the interfaces caused by small interface thickness. So we use the non-uniform adaptive sampling method.

Next, the non-uniform distributed resampling method used in this paper is introduced. The PDE residual (5) is evaluated at residual points, then the value of PDE residual can be used as an indicator for selecting residual points. We periodically stop training to select residual points corresponding to large PDE residual. Then, these points are added to the set of residual points.

Fig. 2 shows one iteration of spatial adaptive resampling. The steps of adaptive sampling in space are illustrated in Algorithm 1.

This method makes more residual points fall into the parts with larger PDE residual and helps PINN to learn the difficult parts better. The approach was proposed in [32] and has been applied to the DeepXDE library to achieve better

computational results. A similar method was introduced in [33]. and applied to solve the phase field equations, overcoming the problem of solving the phase field equations using PINN with fixed residuals.

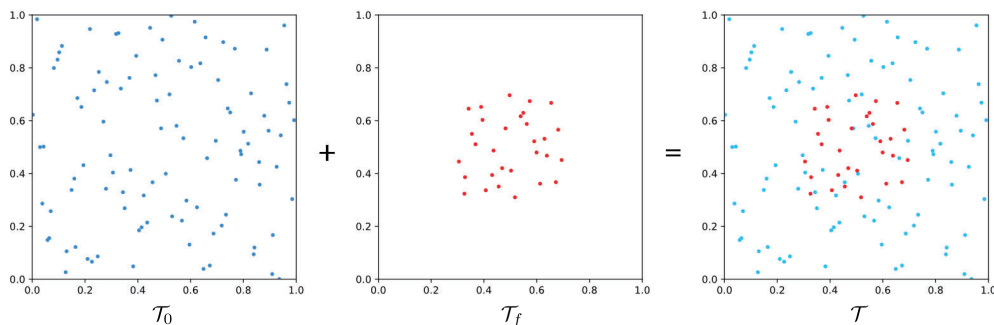


**Fig. 2.** Adaptive sampling in space

---

**Algorithm 1** Adaptive sampling in space

---

- 1: Initialize the parameters of PINN with loss function:  $\mathcal{L} = \mathcal{L}_u + \mathcal{L}_b + \mathcal{L}_r$ ;
  - 2: Sample the initial, boundary and residual points  $\mathcal{T}_0$  using LHS, let  $\mathcal{T} = \mathcal{T}_0$ ;
  - 3: Train the PINN for a certain number of iterations;
  - 4: Select  $m$  points with large residual values as  $\mathcal{T}_f$ , and let  $\mathcal{T} = \mathcal{T} + \mathcal{T}_f$ ;
  - 5: Train the neural network with the points set  $\mathcal{T}$ ;
  - 6: Calculate the mass error;
  - 7: **repeat**
  - 8:     Step 4 ~ 6;
  - 9: **until** The total number of iterations or  $\mathcal{L}$  is no longer reduced
  - 10: **return**  $\hat{u}_\theta(x, t)$ ;
- 

The Cahn-Hilliard equation is a time-dependent partial differential equation. Considering the sharp transitions of the phase pattern and energy with time[33], we don't use a single PINN to predict the solution in full time domain. We decompose the time domain into multiple subintervals and build PINN on each time period to solve it separately which is shown in Fig. 3. For instance, considering the full time domain  $t \in [0, 1]$ , the procedure of adaptive time sampling is illustrated in Algorithm 2.

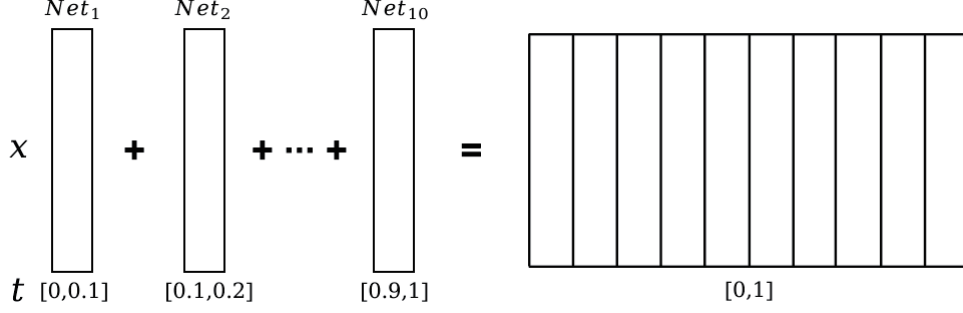


**Fig. 3.** Adaptive sampling in time

---

**Algorithm 2** Adaptive sampling in time

---

- 1: Divide the time domain  $t \in [0, 1]$  into ten subdomains with time step of  $\Delta t = 0.1$ :  $\{[t_n, t_{n+1}]\}_{n=0}^9$ , where  $t_0 = 0$  and  $t_{10} = 1$ ;
  - 2: **for**  $n=1$  to 10 **do**
  - 3:     Initialize the parameters of  $Net_n$  with loss function:  $\mathcal{L}_n = \mathcal{L}_u + \mathcal{L}_b + \mathcal{L}_r$ ;
  - 4:     **if**  $n=1$  **then**
  - 5:         Select the initial conditions of PDEs for  $Net_n$  as initial conditions.
  - 6:     **else**
  - 7:         Select the predicted solution of  $Net_{n-1}$  at time  $t_{n-1}$  for  $Net_n$  as initial conditions.
  - 8:     **end if**
  - 9:     Sample in the subdomain  $[t_{n-1}, t_n] \times \Omega$  to obtain initial points, boundary points and residual points using LHS;
  - 10:     Train  $Net_n$  to converge to an optimal solution;
  - 11: **end for**
  - 12: Concatenate the predicted solutions from each  $Net_n$  in sequential order;
  - 13: **return**  $\hat{u}_\theta(x, t)$ ;
- 

Generally, we divide the entire time domain equally. However, the length of the sub-time domains can be set to be unequal. The time lengths can be larger for the parts that are easy to learn, while the difficult parts are needed carefully handled by choosing smaller time lengths[33].

### 2.2.2. Mass Constraint

Consider the following energy functional:

$$E(u) = \int_{\Omega} \left( \frac{\varepsilon^2}{2} |\nabla u|^2 + F(u) \right) d\mathbf{x}, \quad (6)$$

$u(\mathbf{x}, t)$  is the phase variable,  $\mathbf{x} \in \Omega \subseteq \mathbb{R}^d, t \in [0, T]$ ,  $\varepsilon$  is a positive constant associated with the diffuse interface width,  $F(u)$  is the nonlinear bulk potential.



There are two common types of nonlinear bulk potentials [1, 41–43]:

- Ginzburg-Landau double-well type potential:

$$F_{ab}(u) = \frac{1}{4}(u^2 - 1)^2, \quad u \in (-\infty, +\infty). \quad (7)$$

- Logarithmic Flory-Huggins potential:

$$F_{fh}(u) = (1 + u) \ln(1 + u) + (1 - u) \ln(1 - u) - \frac{\theta}{2}u^2, \quad u \in (-1, 1). \quad (8)$$

For the free energy (6), the Cahn-Hilliard equations are obtained under the  $H^{-1}$  gradient flow, as follows,

$$u_t = \Delta(-\varepsilon^2 \Delta u + f(u)), \quad (9)$$

where  $f(u) = F'(u)$ . Periodic boundary conditions and Neumann boundary conditions are used on area  $\Omega$ . The above Cahn-Hilliard equation has the following properties:

- mass conservation

$$\int_{\Omega} u(\mathbf{x}, t) d\mathbf{x} = \int_{\Omega} u(\mathbf{x}, 0) d\mathbf{x}, \quad \forall t > 0. \quad (10)$$

- energy dissipation

$$E(u(t)) \leq E(u(s)), \quad \forall t \geq s. \quad (11)$$

In experiments, we found that even though the Cahn-Hilliard equation has the property of mass conservation, the mass of the predicted solution of the baseline PINN does not achieve conservation, which also leads to errors, seen in Fig. 4b.

The following is the reason why it fails to achieve mass conservation. When solving the equation (9) by PINN, we generally introduce new variables and rewrite (9) as follows:

$$u_t = \Delta \varphi, \quad (12)$$

$$\varphi = -\varepsilon^2 \Delta u + f(u). \quad (13)$$

This is because neural networks are so costly to compute higher order derivatives by backpropagation. We set the output layer of the neural network to be two neurons that output the predicted values of  $\varphi$  and  $u$ , denoted as  $\hat{\varphi}_{\theta}$  and  $\hat{u}_{\theta}$ , respectively. After that, the residual loss term of the equation takes the following form:

$$\mathcal{L}_r(\theta) = \frac{1}{N_r} \sum_{i=1}^{N_r} \left( \left| \frac{\partial \hat{u}_{\theta}}{\partial t} - \Delta \hat{\varphi}_{\theta} \right|^2 + |\hat{\varphi}_{\theta} - (-\varepsilon^2 \Delta \hat{u}_{\theta} + f(\hat{u}_{\theta}))|^2 \right). \quad (14)$$

We note (12) guarantees the mass conservation property of the equation, while the first term in (14) can only be optimized to be as small as possible but not exactly equal to zero after the neural network training is completed. This results in mass degradation when solving the Cahn-Hilliard equations using the baseline PINN. To solve this problem, we add a constraint of mass to the loss function of the baseline PINN to improve the accuracy of the solution. This is only a soft constraint, which we call mass loss. It is calculated as follows:

$$\mathcal{L}_m(t, \theta) = \frac{1}{N_t} \sum_{i=1}^{N_t} |m(\hat{u}_\theta, t_m^i) - m(u, 0)|^2, \quad (15)$$

where the mass at  $t$  moments  $m(u_\theta, t)$  can be calculated by some numerical integration methods.  $\{\mathbf{x}_q^j, \omega_j\}_{j=1}^{N_q}$  denote the orthogonal points and the corresponding weights in the computational domain  $\Omega$ , respectively, then the mass  $m(\hat{u}_\theta, t_m^i)$  at the moment  $t_m^i$  is calculated as:

$$m(\hat{u}_\theta, t_m^i) = \int_{\Omega} \hat{u}_\theta(\mathbf{x}, t_m^i) d\mathbf{x} \approx \sum_{j=0}^{N_q} \omega_j \hat{u}_\theta(\mathbf{x}_q^j, t_m^i). \quad (16)$$

The above mass loss function (15) is added to the PINN loss function as a regular term. It enables the predicted solutions to maintain the initial mass and also improves the accuracy of the PINN in solving the Cahn-Hilliard equation.

### 2.3. Mass-preserving spatio-temporal adaptive PINN

In this section we show the process of the mass-preserving spatio-temporal adaptive PINN. We mentioned in the section 2.2.2 that the Cahn-Hilliard equation has the properties of energy dissipation and mass conservation. There are time domains where the phase pattern changes rapidly during the evolution, generally associated with the fast decrease of energy.

In section 2.2.1, we mentioned that when employing adaptive sampling in time, the length of the sub-time domain can be adjusted based on the level of difficulty in learning. For the phase field equations, the time domain where the phase structure evolves rapidly is hard to learn, while the slowly changing part is easy to learn. The evolution of the phase structure is consistent with the evolution of the energy, so we divide the full time domain according to the rate of energy decrease. The specific steps are as follows:

First, we divide the entire time region  $[0, T]$  into  $N$  segments of equal length:

$$[T_0, T_1], [T_1, T_2], \dots, [T_{N-1}, T_N], \quad (17)$$

where  $T_0 = 0$ ,  $T_N = T$ . Then establish PINN in each time interval separately:

$$Net_1, Net_2, \dots, Net_N. \quad (18)$$

They can be set to different network structures, for simplicity, the same network structure is used in all experiments in this paper. The initial condition of the equation is selected as the initial condition of  $Net_1$ , and the output of  $Net_n$  ( $n = 1, \dots, N-1$ ) at its final time  $T_n$  is selected as the initial condition of  $Net_{n+1}$ . After a certain number of iterations, the spatial adaptive resampling in section 2.2.1 is used to add residual points to reinforce the training result. After each  $Net_n$  has been sufficiently trained, the solutions on each subdomain are concatenated to obtain the solution in the total time domain, denoted as  $\hat{u}_{crude}$ .

Second, we may need adjust the the time domain division to improve of the accuracy of the solution. If the error values and mass conservation of the crude solution are relatively good, the next step is not necessary. If the error is large or the situation of mass conservation is undesirable, we plot the numerical energy and mass in the full time domain according to the crude solution  $\hat{u}_{crude}$ . Then we find the region where the mass value fluctuates and the energy changes rapidly, which serves as a reference for our next adjustment of the time domain division method. Generally both of the above situations occur simultaneously. The PINN in full time domain cannot simulate this change perfectly, which leads to numerical fluctuations of the mass. We next adjust the length and number of time segments according to the rate of energy decrease. Specifically, small time segments are divided in regions where the energy decreases rapidly, and conversely large time segments are set in regions where the energy decreases slowly. The following Algorithm 3 describes the proposed adaptive PINN:

---

**Algorithm 3** Mass-preserving spatio-temporal adaptive PINN

---

- 1: Divide the time domain equally into  $N$  subdomains;
  - 2: **for**  $n = 1$  to  $N$  **do**
  - 3: Initialize the parameters of PINN with loss function:  $\mathcal{L}_n = \lambda_u \mathcal{L}_u + \mathcal{L}_b + \mathcal{L}_r + \lambda_m \mathcal{L}_m$ ;
  - 4: Sample the initial, boundary and residual points using LHS;
  - 5: Train the PINN for a certain number of iterations;
  - 6: Adaptive resampling in space repeated several times
  - 7: Get the predictions  $\hat{u}_\theta(x, t)$ ;
  - 8: **end for**
  - 9: Plot the numerical energy and mass in the full time domain according to  $\hat{u}_\theta(x, t)$ ;
  - 10: Calculate the mass error;
  - 11: **repeat**
  - 12: Adjust the time domain division according to the rate of energy decrease, and fine-tune the weight of mass loss according to the mass error;
  - 13: Step 2 ~ 8;
  - 14: **until** The total number of iterations or mass error and solution error reach the limit
  - 15: Get the final predicted solutions  $\hat{u}_\theta(x, t)$ ;
  - 16: **return**  $\hat{u}_\theta(x, t)$ ;
-

### 3. Numerical results

In this section, several numerical results for the Cahn-Hilliard equation with different energy potentials will be presented. These results serve to evaluate the ability of the proposed modified method in solving parabolic equations, especially the equations with high order spatial derivatives and singular energy functionals, as well as the effect of dimensionality. It will be illustrated by the solution errors and the mass error.

The reference solutions  $u$  for the following numerical results were obtained using classical numerical methods, employing a semi-implicit discretization in time and spectral method in space. The accuracy of the predicted solution  $\hat{u}_\theta$  is measured by the absolute error and relative  $L^2$  error, computed on the data point set  $\{(\mathbf{x}_i, t)\}_{i=1}^N \in \Omega \times [0, T]$ .

The absolute error at time  $t$  is:

$$Error_{abs}(\mathbf{x}_i, t) = |\hat{u}_\theta(\mathbf{x}_i, t) - u(\mathbf{x}_i, t)|. \quad (19)$$

The relative  $L^2$  error at time  $t$  is:

$$Error_{L^2} = \frac{\sqrt{\sum_{i=1}^N |\hat{u}_\theta(\mathbf{x}_i, t) - u(\mathbf{x}_i, t)|^2}}{\sqrt{\sum_{i=1}^N |u(\mathbf{x}_i, t)|^2}}. \quad (20)$$

The conservation of mass is measured by the mass error, which is defined as follows:

$$Error_{mass} = |m(\hat{u}_\theta(\mathbf{x}, t)) - m(u_0)|. \quad (21)$$

In the rest of this section, we first test the fourth order Cahn-Hilliard equation with Ginzburg-Landau potential, demonstrating the operation details and effectiveness of this method. Then, we extend its application to solve the Cahn-Hilliard equation with Flory-Huggins potential, which exhibits singularity. Finally, in order to further validate the effect of the mass-preserving spatio-temporal adaptive PINN, we apply the method to more complex phase field models by simulating the system of Cahn-Hilliard equations and a three-dimensional Cahn-Hilliard equation.

#### 3.1. Cahn-Hilliard equation with Ginzburg-Landau potential in two dimensions(2D)

We start by testing a relatively simple case, which is the 2D Cahn-Hilliard equation with the polynomial Ginzburg-Landau potential. In this example, we consider the equation given by

$$\begin{cases} u_t = \Delta\varphi, & (x, y) \in [-1, 1]^2, \quad t \in [0, 1], \\ \varphi = -\varepsilon^2 \Delta u + (u^3 - u), \end{cases} \quad (22)$$

with periodic boundary conditions, the parameter  $\varepsilon = 0.05$ , and the initial profile for  $u$  as

$$u(x, y, t = 0) = \max \left( \tanh \frac{r - R_1}{2\varepsilon}, \tanh \frac{r - R_2}{2\varepsilon} \right), \quad (23)$$

where  $r = 0.4$ ,  $R_1 = \sqrt{(x - 0.7r)^2 + y^2}$ ,  $R_2 = \sqrt{(x + 0.7r)^2 + y^2}$ . This initial condition consists of two circles and we will simulate the process of their merging. First, we consider the case without a mass loss term, choose the time step  $\Delta t = 0.2$  to divide the time domain  $t \in [0, 1]$  into five subdomains. Feedforward fully connected neural networks are established in each subdomain separately, and each network have 10 hidden layers with 50 neurons per layer, along with two outputs. The hyperbolic tangent function is chosen for the activation function, and the loss function for each network is defined as follows:

$$\left\{ \begin{array}{l} \mathcal{L} = \lambda_u \mathcal{L}_u + \mathcal{L}_b + \mathcal{L}_r, \\ \mathcal{L}_u = \frac{1}{N_u} \sum_{i=1}^{N_u} |\hat{u}_\theta(\mathbf{x}_u^i, 0) - u_i|^2, \\ \mathcal{L}_b = \frac{1}{N_b} \sum_{i=1}^{N_b} (|\hat{u}_\theta(\mathbf{x}_u^i, t_b^i) - \hat{u}_\theta(\mathbf{x}_l^i, t_b^i)|^2 + \left| \frac{\partial \hat{u}_\theta}{\partial \mathbf{x}}(\mathbf{x}_u^i, t_b^i) - \frac{\partial \hat{u}_\theta}{\partial \mathbf{x}}(\mathbf{x}_l^i, t_b^i) \right|^2), \\ \mathcal{L}_r = \frac{1}{N_r} \sum_{i=1}^{N_r} (|\hat{\varphi}_\theta(\mathbf{x}_r^i, t_r^i) + \varepsilon^2 \Delta \hat{u}_\theta(\mathbf{x}_r^i, t_r^i) - (\hat{u}_\theta(\mathbf{x}_r^i, t_r^i)^3 - \hat{u}_\theta(\mathbf{x}_r^i, t_r^i))|^2 \\ + \left| \frac{\partial \hat{u}_\theta}{\partial t}(\mathbf{x}_r^i, t_r^i) - \Delta \hat{\varphi}_\theta(\mathbf{x}_r^i, t_r^i) \right|^2). \end{array} \right. \quad (24)$$

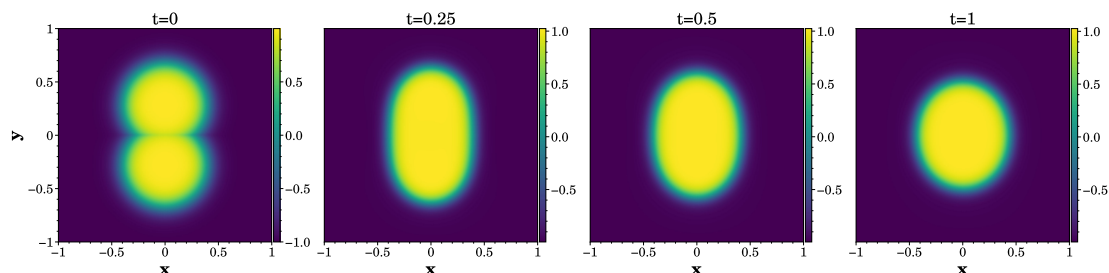
In this experiment, 10000 initial points, 1600 boundary points, and 20000 residual points are used for training. The weight  $\lambda_u$  of the initial condition is set to 100, with all other weights are 1. To train the neural network, we first use the Adam optimizer with a learning rate of 0.001, and then the L-BFGS-B optimizer to fine-tune the neural network.

Adaptive resampling in space is performed every 5000 steps of training, and each time 1000 residual points with large residual value are selected to be added to the initial set of residual points. After experimental testing, we chose to perform three times spatial adaptive resampling because the accuracy and computational cost are optimal in this case.

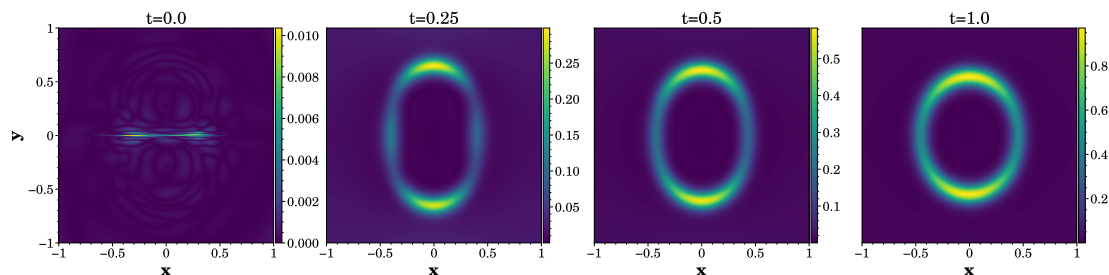
The predicted solutions at different times ( $t = 0, 0.25, 0.5, 1$ ) are shown in Fig. 4(a), and the absolute errors between the predicted and reference solutions are shown in Fig. 4(b). Fig. 4(a) and Fig. 4(b) show that although we can capture the phenomenon of two circles merging, the maximum absolute errors of the predicted

solutions are large, with values of 0.298, 0.583, and 0.971. The absolute error increases with time evolving. So the algorithm needs further improvement to reduce the absolute errors.

The variation of energy and mass with time are shown in Fig. 5(a) and Fig. 5(b), we can observe that the mass is not conserved although the energy stays decreasing. The decrease in the area of the yellow region in Fig. 4(a) also indicates that the mass is not conserved. Since the original physical system has the property of mass conservation, while the predictions of PINN do not conform to this principle, adjustments are necessary to ensure that the PINN satisfies the physical laws.



(a) Predicted solutions at  $t = 0, 0.25, 0.5, 1$



(b) Absolute errors at  $t = 0, 0.25, 0.5, 1$

**Fig. 4.** Predicted solutions and relative errors of 2D Cahn-Hilliard equation with Ginzburg-Landau potential given by spatio-temporal adaptive PINN with time step  $\Delta t = 0.2$ .

Therefore, we add the following mass loss term  $\mathcal{L}_m$  to the total loss function for each PINN:

$$\mathcal{L}_m = \frac{1}{N_t} \sum_{i=1}^{N_t} |m(\hat{u}_\theta, t_m^i) - m(u, 0)|^2, \quad (25)$$

where

$$m(u, t) = \int_{\Omega} u d\mathbf{x} \approx \frac{1}{N_q} \sum_{j=1}^{N_q} u(\mathbf{x}_q^j, t). \quad (26)$$

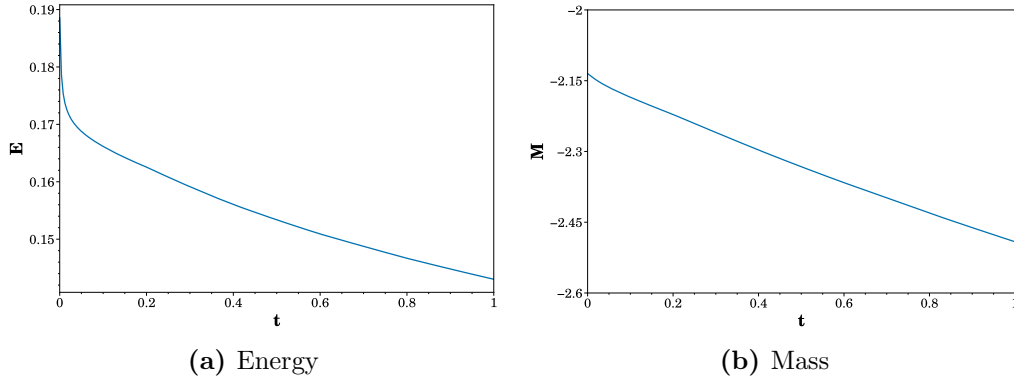


**Fig. 5.** The numerical energy( $E$ ) and mass( $M$ ) of the predicted solutions  $\hat{u}_\theta(\mathbf{x}, t)$

We choose  $N_t = 21$  equidistant points in each time subdomain as  $t_m^i$  in Eq.(25), and the mass at each moment  $t_i$  is computed at  $50 \times 50$  quadrature points  $\{(\mathbf{x}_q^j, y_q^j)\}_{j=1}^{N_q}$ . The predicted solutions and absolute errors are shown in Fig. 6(a) and Fig. 6(b). From Fig. 6(b), it is observed that the maximum absolute error of each moment decreases to 0.084, 0.056 and 0.044, which are smaller than the absolute errors in Fig. 4(b).

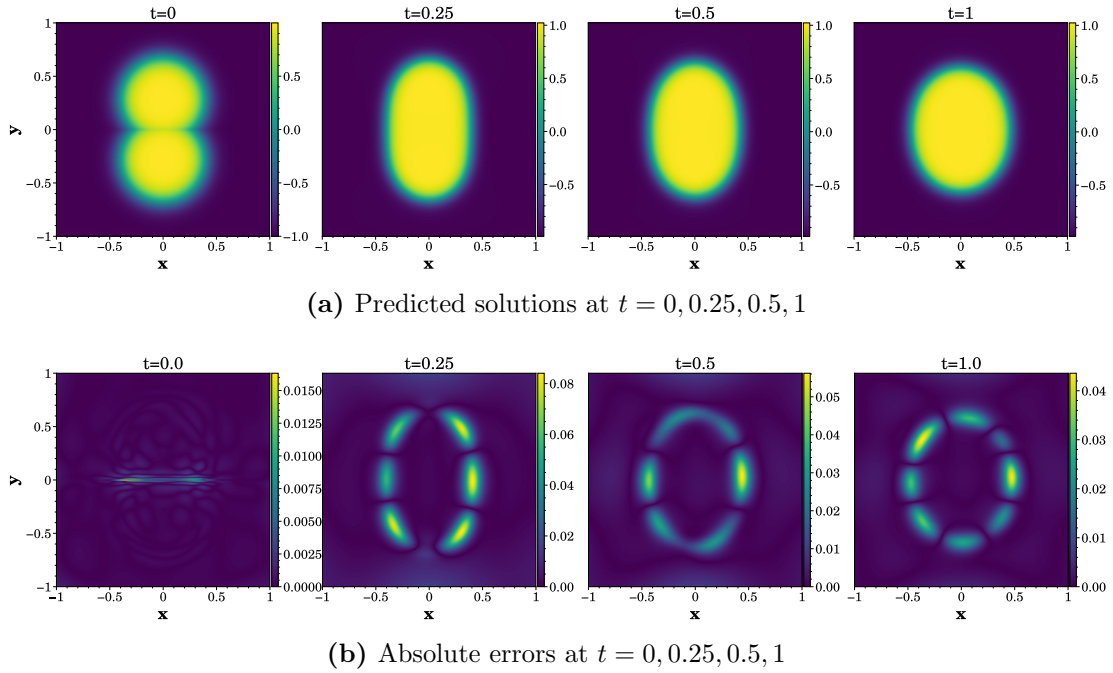


**Fig. 6.** Predicted solutions and absolute errors of 2D Cahn-Hilliard equation with Ginzburg-Landau potential obtained by adding the mass loss while using adaptive sampling approach.

After adding the mass loss function, the evolutions of energy and mass are plotted in Fig. 7(a) and Fig. 7(b). The results show that the energy of the predicted solutions decreases with time. The value of the mass is relatively stable in the later stages, while the mass error in the initial stage is large, with a maximum value of  $2.27\text{e-}03$  in the entire time domain.

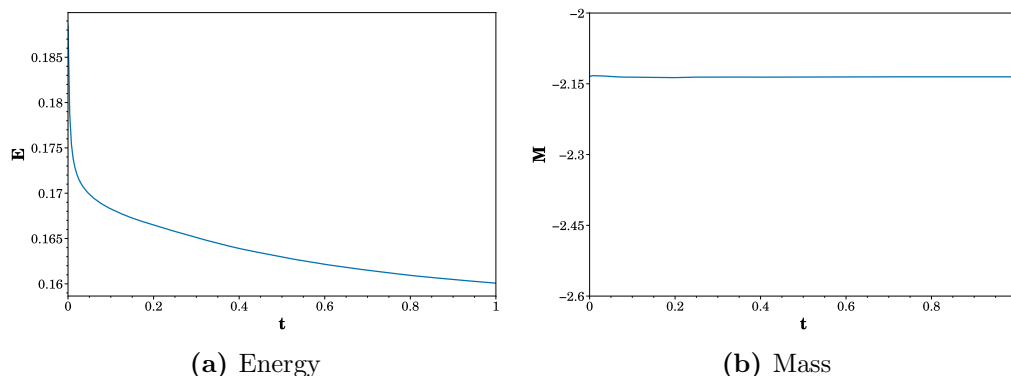
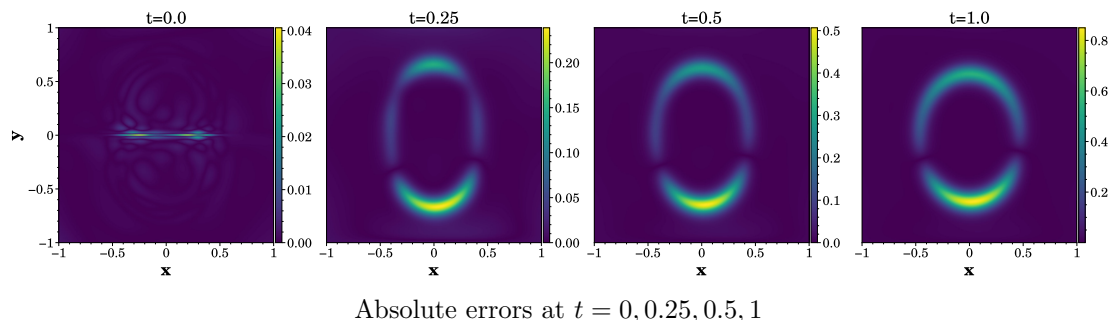


**Fig. 7.** The numerical energy( $E$ ) and mass( $M$ ) of the predicted solutions  $\hat{u}_\theta(\mathbf{x}, t)$

To reduce the mass error at the beginning, time segments lengths are adjusted according to the variation of energy with time. Specifically, it is observed that the energy decreases rapidly mainly in  $t \in [0, 0.02]$  and then decreases slowly. Finally, the energy tends to be constant after  $t = 0.2$ . Therefore we reset the length of the time segments to be 0.02, 0.18, 0.4, 0.4, and  $N_t = 26$ . The absolute errors are plotted in Fig. 8. The maximum absolute errors in Fig. 8 are 0.239, 0.507 and 0.849, respectively. The absolute errors are substantially higher compared to those of the above uniform time domain division.



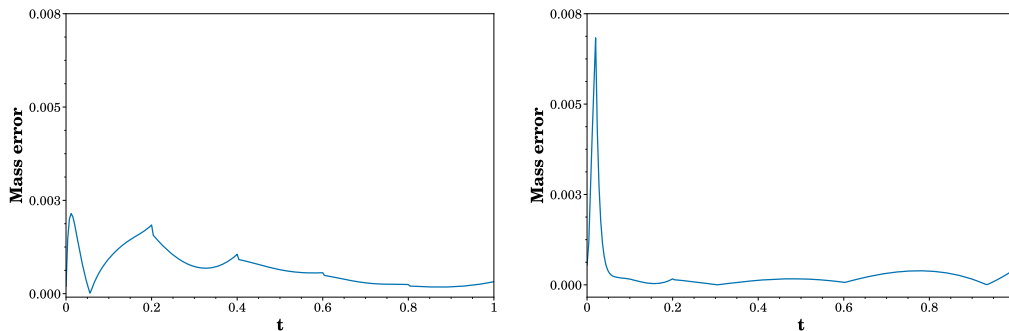
Absolute errors at  $t = 0, 0.25, 0.5, 1$

**Fig. 8.** The absolute errors obtained by using the adaptive sampling approach and adding mass loss, where we chose time steps of 0.02, 0.18, 0.4, 0.4, respectively

We further plot the numerical mass error with two methods of time domain division, shown in Fig. 9(a) and Fig. 9(b). Fig. 9 demonstrates that the maximum mass error of the non-uniform segmentation is larger than one of the uniform segmentation, which reaches  $7.29\text{e-}03$ , but its mass error is mainly concentrated



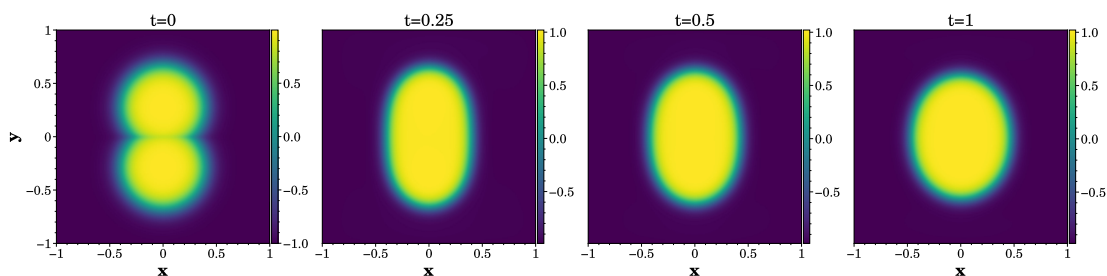
in the initial stage of  $t \in [0, 0.02]$  with a much smaller mass error in the later stage. The simulation results will have some errors at the junction point, which is manifested as the fluctuation of the mass curve at the junction of two intervals. In order to reduce this fluctuation, too more splitting of intervals are not considered.



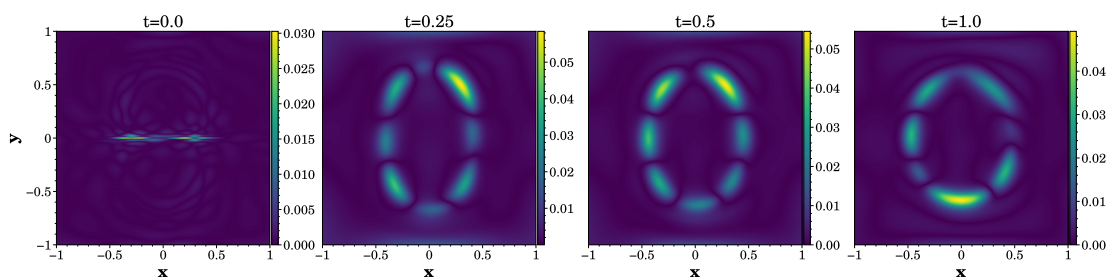
(a) Mass error of uniform segmentation (b) Mass error of non-uniform segmentation

**Fig. 9.** The numerical mass error for two different time domain division methods

With the same non-uniform time domain division above mentioned, we change the weight of mass loss in the first time interval to 10, and keep the others as 1. The predicted solutions and absolute errors are shown in Fig. 10(a) and Fig. 10(b).



(a) Predicted solutions at  $t = 0, 0.25, 0.5, 1$



(b) Absolute errors at  $t = 0, 0.25, 0.5, 1$

**Fig. 10.** With time segments of 0.02, 0.18, 0.4, 0.4, the weight of mass loss in the first time interval is changed to 10 and keep the others as 1, then obtain the predicted solutions and absolute errors of 2D Cahn-Hilliard equation with Ginzburg-Landau potential.

The maximum absolute errors of each time in Fig. 10(b) are 0.058, 0.054 and 0.049. Although the maximum absolute errors are not improved significantly compared to one with the uniform time domain division, the maximum mass error is reduced to 1.01e-03.

The numerical energy and mass are shown in Fig. 11(a) and Fig. 11(b). Fig. 11(b) illustrates that the law of mass conservation is preserved exactly.

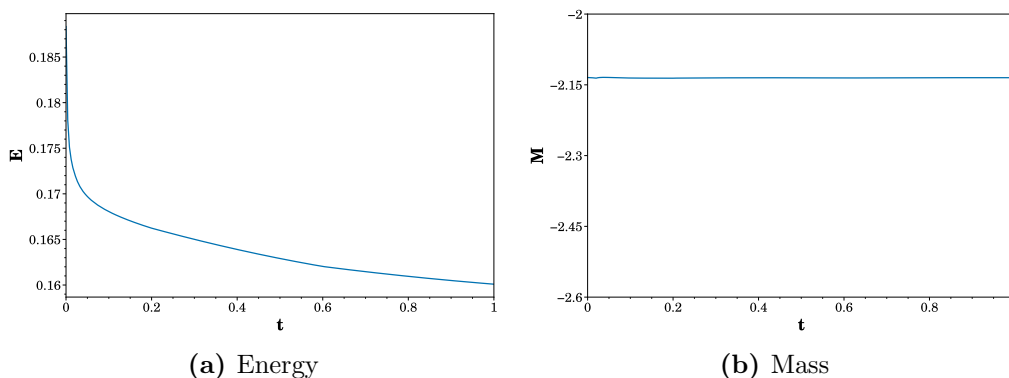


**Fig. 11.** The numerical energy( $E$ ) and mass( $M$ ) of the predicted solutions  $\hat{u}_\theta(\mathbf{x}, t)$

A comparison of the relative  $L^2$  errors and maximum mass errors is shown in Table 1. In Table 1,  $err_1$  represents the errors obtained by solving the equation (22) only by using adaptive sampling in time and space with uniform time domain division, and  $err_2$  are errors obtained by adding a mass constraint to the  $err_1$  operation.  $err_3$  adjusts the time step to be non-uniform with all other operations being the same. The errors in  $err_4$  are obtained by further adjusting the mass loss weights based on the operation of  $err_3$ . We change the mass loss weight to 10 for the first interval and keep the weights for the other intervals as 1.

**Table 1**

Cahn-Hilliard equation with Ginzburg-Landau potential: relative  $L^2$  errors and maximum mass error of four cases at different times

Time	$err_1$	$err_2$	$err_3$	$err_4$
0	5.23e-04	7.26e-04	1.86e-03	1.39e-03
0.25	5.10e-02	1.59e-02	3.46e-02	8.36e-03
0.5	1.12e-01	8.34e-03	7.34e-02	8.40e-03
1	2.15e-01	7.13e-03	1.41e-01	7.10e-03
mass error	3.56e-01	2.27e-03	7.29e-03	1.01e-03

It is illustrated by Table 1 that the relative  $L^2$  error at each time is the lowest when using the mass-preserving spatio-temporal adaptive PINN method. The

maximum mass error is also the smallest. We note that such a process can be well applied to a large class of complex parabolic equations, especially phase field equations. Although the reduction of error by this procedure is not significant for the case of Ginzburg-Landau potential, it is important for Flory-Huggins potential. It significantly reduces the absolute errors of the predicted solutions and guarantees mass conservation, which will be shown in the following.

### 3.2. Cahn-Hilliard equation with Flory-Huggins potential in two dimensions(2D)

In this section, we tested the 2D Cahn-Hilliard equation with Flory-Huggins potential. It has a highly nonlinear and singular energy potential, so we need to reduce the error due to singularity. The solution domain for the numerical example is  $\Omega := [-1, 1]^2$ ,  $t \in [0, 1]$ . We mainly focused on the following specific form,

$$\begin{cases} u_t = \Delta\varphi, \\ \varphi = -\varepsilon^2\Delta u + (\ln(1+u) - \ln(1-u) - \theta u), \end{cases} \quad (27)$$

with periodic boundary conditions. We set  $\varepsilon = 0.05$ ,  $\theta = 3$ , along with the initial condition

$$u(x, y, t = 0) = \max\left(\tanh\frac{r-R_1}{2\varepsilon}, \tanh\frac{r-R_2}{2\varepsilon}\right) \times 0.9, \quad (28)$$

where  $r = 0.4$ ,  $R_1 = \sqrt{(x-0.7r)^2 + y^2}$ ,  $R_2 = \sqrt{(x+0.7r)^2 + y^2}$ .

The Ginzburg Landau potential energy is in polynomial form and does not require special handling in computations. But the Flory-Huggins potential contains logarithmic terms, and the result will blow up as  $u$  approaches  $\pm 1$  due to its singularity. Therefore, we usually truncate  $u$  at each time step to ensure that its value does not approach  $\pm 1$ , when using the traditional numerical methods. When using PINN to solve problems with singularity, gradient explosion occurs during network training. This is mainly caused by the logarithmic term in the residual loss of the equation. Therefore, we add a mapping to the output of the network such that the value of the output  $u$  is restricted to  $[-0.9, 0.9]$  to avoid the blow up produced by the logarithmic term. The mapping is represented as follows:

$$u_{map} = 1.8 \times \text{sigmoid}(u) - 0.9. \quad (29)$$

First, we use the same network hyperparameters as in the experiments of Section 3.1 and divide the entire time domain equally into five subdomains, with five sub-networks established. Each sub-network performs 3 resampling iterations, with  $N_t = 21$ . The predicted solutions are summarized in Fig. 12(a), and the absolute errors are shown in Fig. 12(b). From Fig. 12(b), the maximum absolute errors of the predicted solutions at different times ( $t = 0.25, 0.5, 1$ ) are 0.109, 0.092

and 0.049, respectively. These errors are much larger than the maximum absolute errors obtained in Section 3.1, which also uses uniform time domain division.

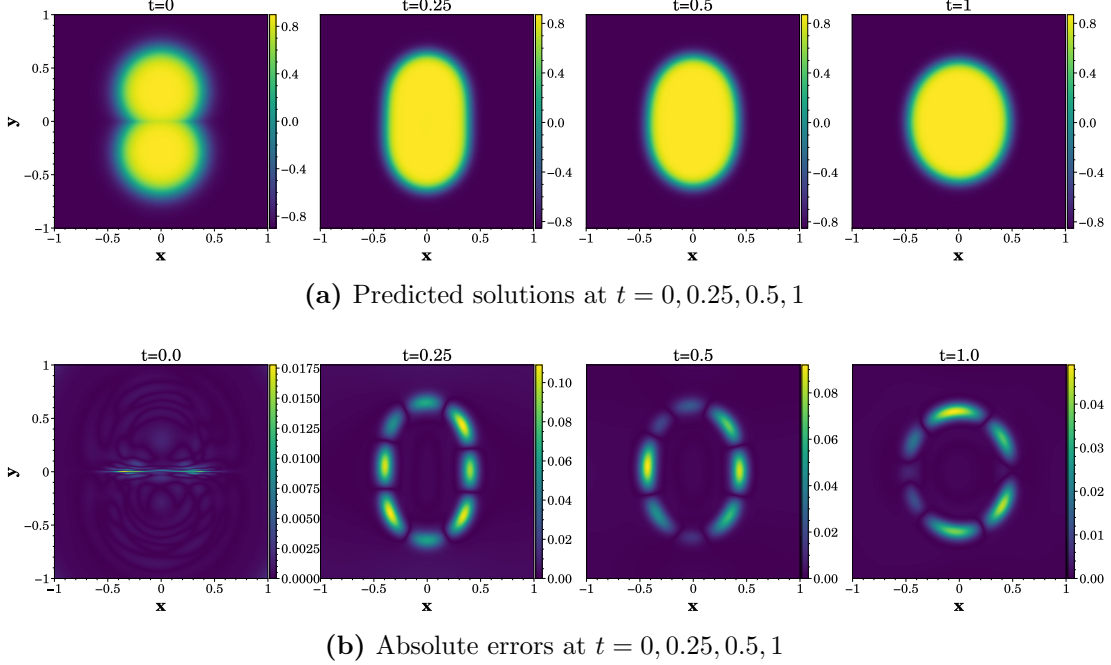


**Fig. 12.** Predicted solutions and absolute errors of 2D Cahn-Hilliard equation with Flory-Huggins potential obtained by adaptive PINN. We add the mass loss and use adaptive sampling approach in space and time. The time domain is divided uniformly, with  $\Delta t = 0.2$ .

Based on the predicted solutions above, we plot the numerical energy and mass within  $t \in [0, 1]$  in Fig. 13(a) and Fig. 13(b). In Fig. 13(b), it is illustrated that the mass fluctuates significantly within  $t \in [0, 0.4]$  and has a numerical jump at the junction of the two time intervals. Attempts to increase the parameter  $N_t$  of mass loss to maintain mass conservation are also ineffective. Fig. 13(a) shows that the energy decreases rapidly at the initial moment, indicating that the merging of the two circles at the initial moment is so fast that the neural networks based on the uniform time domain division could not capture the process perfectly. Next we adjust the length of the time segments according to the rate of energy decrease.

From Fig. 13(a), the energy decreases sharply in  $t \in [0, 0.05]$  and the mass value also fluctuation severely in  $t \in [0, 0.05]$ . It is indicated that the solution changes rapidly in this time period, which is the difficult part for the neural network to learn. The energy decreasing trend in  $t \in [0.05, 1]$  becomes slower, which is the easy part to learn. To address the issue of mass non-conservation at the initial stage, the time domain division is adjusted according to the energy variation.

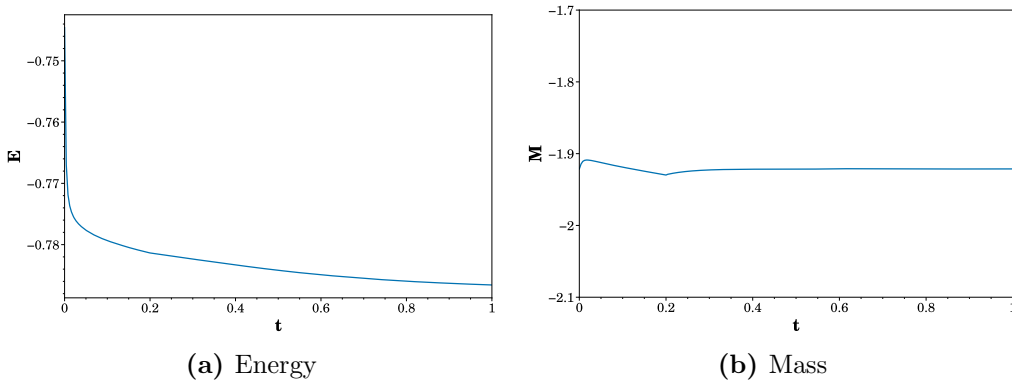


**Fig. 13.** The numerical energy( $E$ ) and mass( $M$ ) of the predicted solutions  $\hat{u}_\theta(\mathbf{x}, t)$

We choose the time segment lengths to be 0.05, 0.15, 0.4 and 0.4, with  $N_t = 26$  for mass loss. The other parameters are the same as above. Fig. 14 shows the predicted solutions and its absolute errors. The maximum absolute errors of the predicted solutions at each moment are 0.064, 0.048 and 0.078, respectively. The maximum absolute error at  $t = 0.25$  decreases slightly compared to the result in Fig. 12(b). The magnitude of the errors are similar for both of them at the later stage. This suggests that our practice of adjusting the length of the time interval is effective since it improves the accuracy of the solution near the initial stage.

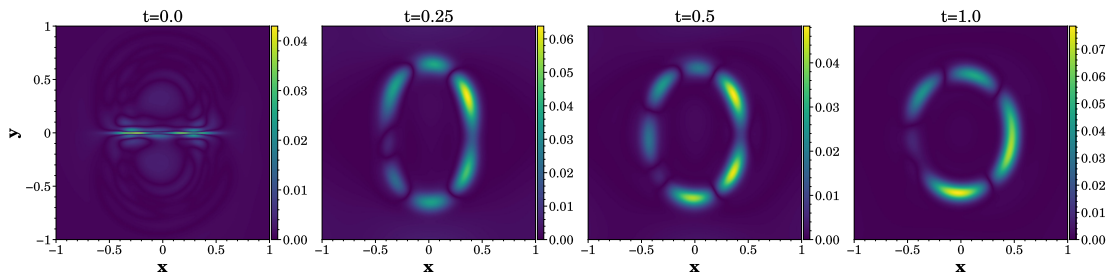
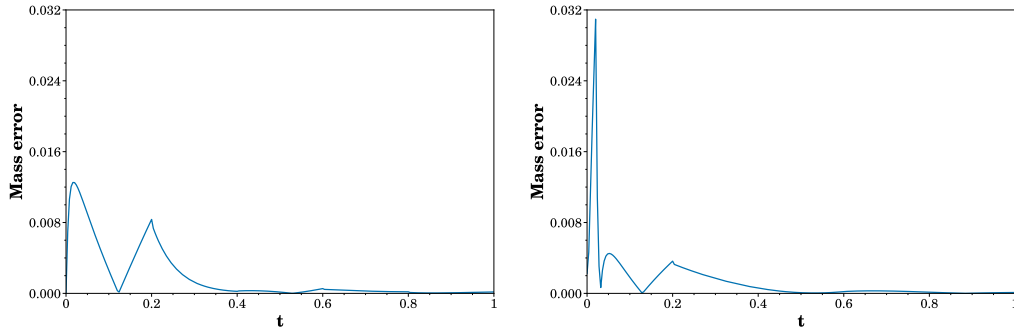


**Fig. 14.** Absolute errors of 2D Cahn-Hilliard equation with Flory-Huggins potential at  $t = 0, 0.25, 0.5, 1$ . We adjust the time-domain decomposition according to the rate of energy decrease. The lengths of the time segments are 0.05, 0.15, 0.4 and 0.4.

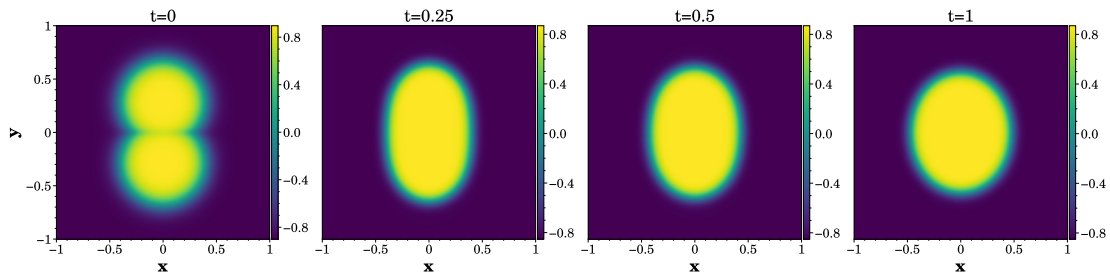
The numerical mass error of the predicted solutions for the two different time domain division methods are shown in Fig. 15(a) and Fig. 15(b). The mass error obtained by non-uniform segmentation approach is large within  $t \in [0, 0.02]$ , but is much smaller in the subsequent time domain than ones obtained by uniform segmentation.



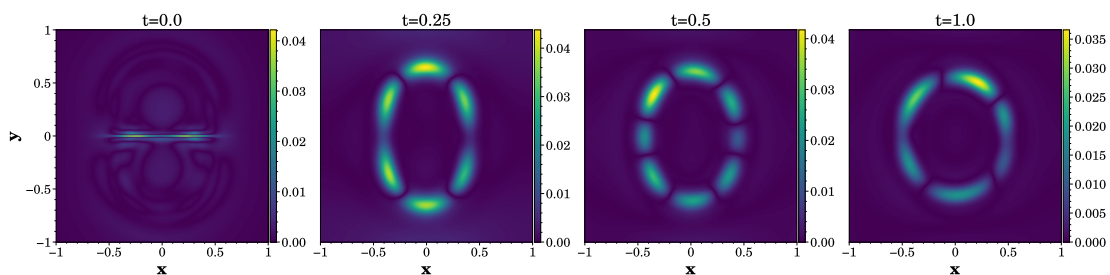
(a) Mass error of uniform segmentation (b) Mass error of non-uniform segmentation

**Fig. 15.** The numerical mass error for two different time domain division methods

As in the previous section, we no longer divide the intervals to avoid the accumulation of errors. The mass error in Fig. 15(b) are mainly concentrated in the first interval, so the weights of mass loss for each network are set to 50, 10, 10, and 10, and  $N_t = 51$ . The predicted solutions and the absolute errors are shown in Fig. 16(a) and Fig. 16(b). The maximum absolute errors of the predicted solutions at different times ( $t = 0.25, 0.5, 1$ ) are 0.044, 0.042, and 0.037, which are greatly reduced compared to the simulation results based on the uniform time interval.



(a) Predict solutions at  $t = 0, 0.25, 0.5, 1$



(b) Absolute error at  $t = 0, 0.25, 0.5, 1$

**Fig. 16.** Predicted solutions and absolute errors of 2D Cahn-Hilliard equation with Flory-Huggins potential obtained by adaptive PINN. The mass loss weight of PINN in each interval is changed to 50, 10, 10, and 10.

The numerical energy and mass are plotted in Fig. 17(a) and Fig. 17(b). The maximum mass error decreases to  $1.65\text{e-}03$ , and the maximum absolute errors of the predictions are greatly reduced. From the above experimental results, it can be seen that the computational accuracy of the predicted solution at the initial moment is important for long time simulations.

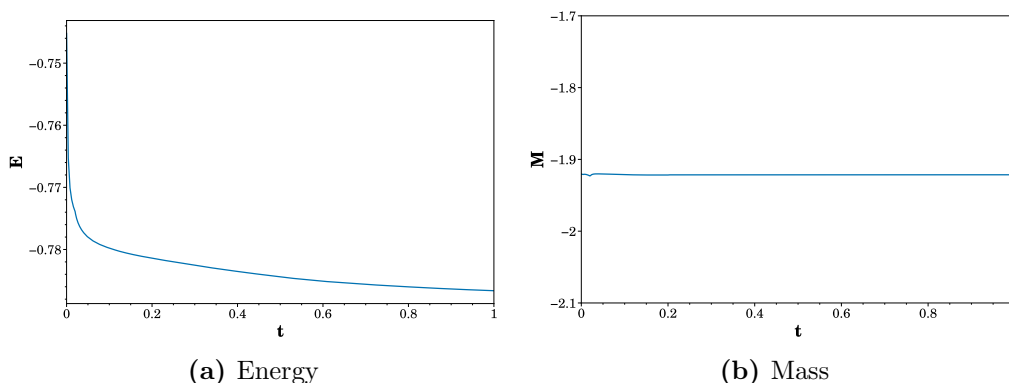


**Fig. 17.** The numerical energy( $E$ ) and mass( $M$ ) of the predicted solutions  $\hat{u}_\theta(\mathbf{x}, t)$

A comparison of the relative  $L^2$  errors and maximum mass errors is shown in Table 2. In  $err_1$ , mass loss is added and the adaptive sampling method is used, with a uniform time domain division for the full time domain.  $err_2$  denotes the errors obtained by non-uniform time domain division. Finally, the weight of mass loss is further adjusted based on the non-uniform time domain division to obtain errors as  $err_3$ .

**Table 2**

Cahn-Hilliard equation with Flory-Huggins potential: relative  $L^2$  errors and maximum mass errors of three cases at different times

Time	$err_1$	$err_2$	$err_3$
0	$9.38\text{e-}04$	$2.79\text{e-}03$	$2.69\text{e-}03$
0.25	$2.24\text{e-}02$	$1.05\text{e-}02$	$9.30\text{e-}03$
0.5	$1.50\text{e-}02$	$8.52\text{e-}03$	$6.97\text{e-}03$
1	$8.39\text{e-}03$	$1.38\text{e-}02$	$5.75\text{e-}03$
mass error	$1.25\text{e-}02$	$3.10\text{e-}02$	$1.65\text{e-}03$

Table 2 illustrates that we have the smallest relative  $L^2$  error and maximum mass error for each moment after using the mass-preserving spatio-temporal adaptive method. For the Cahn-Hilliard equation with Flory-Huggins potential, this method is significantly effective. It greatly reduces the absolute errors of the predicted solutions and guarantees mass conservation.

### 3.3. Simulations for the high-dimensional Cahn-Hilliard equation and the system of Cahn-Hilliard equations

#### 3.3.1. Cahn-Hilliard equation with Flory-Huggins potential in three dimensions(3D)

In this section, we test 3D Cahn-Hilliard equation with Flory-Huggins potential to check the ability of the algorithm to simulate high dimensional problems. The solution domain for this numerical example is  $\Omega := [0, 1]^3$ ,  $t \in [0, 1]$ . The system is summarized as follows:

$$\begin{cases} u_t = \Delta\varphi, \\ \varphi = -\varepsilon^2\Delta u + (\ln(1+u) - \ln(1-u) - \theta u). \end{cases} \quad (30)$$

We chose the periodic boundary conditions, and set the parameters as  $\varepsilon = 0.05$ ,  $\theta = 3$ . The initial condition consists of two spheres,

$$\begin{cases} u(x, y, z; t = 0) = \max\left(\tanh\frac{0.26 - R_1}{2\varepsilon}, \tanh\frac{0.26 - R_2}{2\varepsilon}\right), \\ R_1 = \sqrt{(x - 0.5)^2 + (y - 0.5)^2 + (z - 0.66)^2}, \\ R_2 = \sqrt{(x - 0.5)^2 + (y - 0.5)^2 + (z - 0.34)^2}. \end{cases} \quad (31)$$

In this experiment, 10,000 initial points, 1,600 boundary points, and 20,000 residual points are used for training. Finally, we set the mass loss weight to be 10 for the first time subdomain and 1 for the others. The weight  $\lambda_u$  of the initial condition is set to 100, and all others are 1. To train the neural network, we first use the Adam optimizer with a learning rate of 0.0005, then the L-BFGS-B optimizer to fine-tune the neural network.

Adaptive resampling in space was performed every 5000 steps of training, and each time 1000 residual points with large residuals of the equation were chosen and added to the initial set of residual points. This procedure is performed three times for each sub-time domain. The mapping proposed in Section 3.2 is added for the output of the network to prevent the gradient explosion due to the singularity. The time domain is divided into four segments, namely with lengths of 0.02, 0.18, 0.4, and 0.4.

The predicted solutions at different times ( $t = 0, 0.25, 0.5, 1$ ) are shown in Fig. 18, showing the merging process from two balls into one. The reference solutions are computed by using a spatial discretisation mesh of  $64 \times 64 \times 64$  and time step of  $\Delta t = 1e^{-5}$ . The magnitude of the absolute errors are similar to one of the two dimensional case, namely  $O(1)$ . Based on the predicted solutions above, the numerical energy and mass within  $t \in [0, 1]$  are plotted in Fig. 19(a) and Fig. 19(b). The maximum mass error is  $6.85e-03$ , which is relatively reasonable.



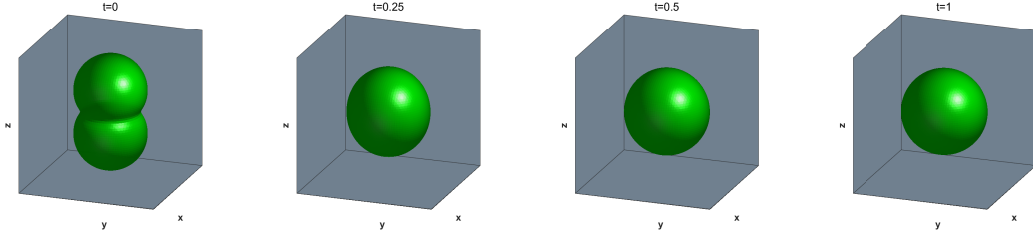


**Fig. 18.** Predicted solutions at  $t = 0, 0.25, 0.5, 1$ . The lengths of the time segments are 0.02, 0.18, 0.4 and 0.4, respectively. The 3D surface is plotted by points in 3D space with the value 0.

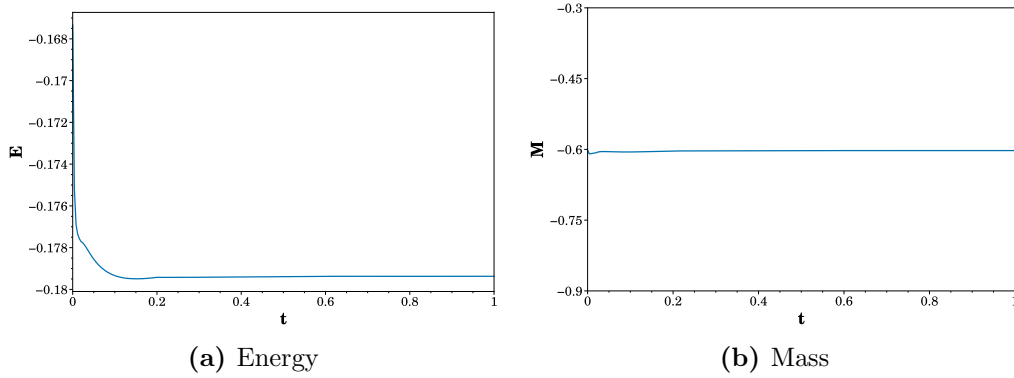


**Fig. 19.** The numerical energy( $E$ ) and mass( $M$ ) of the predicted solutions  $\hat{u}_\theta(\mathbf{x}, t)$

The energy of the system first decreases and then tends to stable with time. The predicted solutions preserve mass conservation. Similar results are obtained from the simulation of the Cahn-Hilliard equation with Ginzburg-Landau potential in three dimensions. From the above simulation, we conclude that the algorithm achieves a satisfactory level of simulation for the 3D Cahn-Hilliard equation.

### 3.3.2. System of Cahn-Hilliard equations in two dimensions

Next, we simulate the two-dimensional system of Cahn-Hilliard equations with coupling terms, which is used to describe the confined binary blended polymers[44–46]. The energy functional of the system is the following expression:

$$E(u) = \int_{\Omega} \left( \frac{\varepsilon_u^2}{2} |\nabla u|^2 + \frac{\varepsilon_v^2}{2} |\nabla v|^2 + W(u, v) \right) d\mathbf{x}, \quad (32)$$

where

$$W(u, v) = \frac{(u^2 - 1)^2}{4} + \frac{(v^2 - 1)^2}{4} + \alpha uv + \beta uv^2. \quad (33)$$

It is a mixture of two systems, including macrophase separation and microphase separation. The order parameter  $u$  represents macrophase separation and  $v$  represents microphase separation. Parameters  $\varepsilon_u$  and  $\varepsilon_v$  control the width of the interface between macrophase and microphase. In equation (33), the coupling parameter  $\alpha$  controls the hydrophilicity of the microscopic phase,  $\beta$  controls the formation of the restricted interface. For the energy functional(32), two coupled Cahn-Hilliard equations are obtained under the  $H^{-1}$  gradient flow, as follows:

$$\begin{cases} u_t = \Delta(-\varepsilon_u^2 \Delta u + u^3 - u + \alpha v + \beta v^2), \\ v_t = \Delta(-\varepsilon_v^2 \Delta v + v^3 - v + \alpha u + 2\beta uv), \end{cases} \quad (34)$$

with periodic boundary conditions. The solution domain is  $\Omega := [0, 1]^2$ ,  $t \in [0, 1]$ , and  $\varepsilon_u = \varepsilon_v = 0.05$ . The coupling parameters as  $\alpha = 0$ ,  $\beta = -0.5$ , meaning that the two components of the microphase have the same hydrophilicity. For this case, we chose the initial condition of  $u$  as a circle and the initial condition of  $v$  as two circles along the diagonal of the solution domain:

$$\begin{cases} u(x, y; t = 0) = \tanh\left(\frac{0.6 - \sqrt{x^2 + y^2}}{2\varepsilon_u}\right), \\ v(x, y; t = 0) = \tanh\left(\frac{0.4 - R_1}{2\varepsilon_v}\right) - \tanh\left(\frac{0.4 - R_2}{2\varepsilon_v}\right), \\ R_1 = \sqrt{(x + 0.25)^2 + (y + 0.25)^2}, \\ R_2 = \sqrt{(x - 0.25)^2 + (y - 0.25)^2}. \end{cases} \quad (35)$$

In this example, we use a neural network consists of 10 hidden layers, with 50 neurons per layer. The above system is transformed into a system of four second order differential equations. Then we set the relevant residual loss functions. The number of sampling points for  $u$  and  $v$  is the same, with 10000 initial points, 1600 boundary points and 20000 residual points. The lengths of the time segments are 0.05, 0.15, 0.4, 0.2 and 0.2, and other settings are the same as before.

Fig. 20(a) shows the transition of the confined interface between polymers and solution. The structure of polymers, represented by the yellow region, changes from a circle to two semicircles. In Fig. 20(b), the yellow and blue regions in the centre have values of 1 and  $-1$ , representing the two kinds of polymers. The external region has a value of 0, representing the solution. The microphase transitions are then observed and contained by the confined interface. Eventually, each polymer occupies one-half of the confined domain, forming a half-sphere structure in the interior.

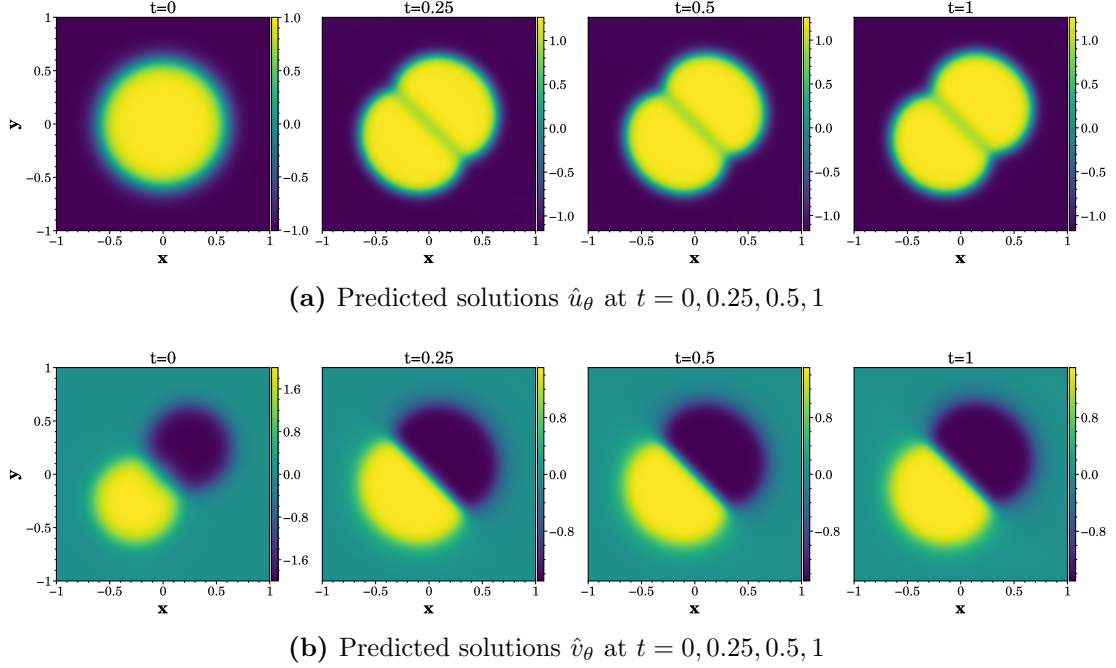


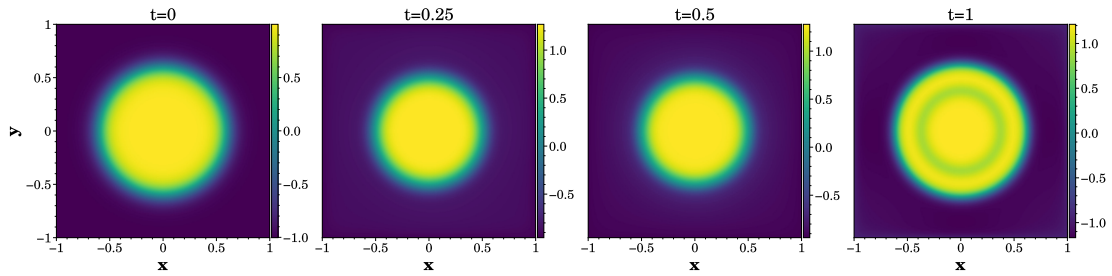
**Fig. 20.** Predicted solutions  $\hat{u}_\theta$  and  $\hat{v}_\theta$  obtained by adaptive PINNs with time segments lengths of 0.05, 0.15, 0.4, 0.2 and 0.2

Next, we simulated the case of hydrophilicity, namely  $\alpha = 0.05$  and  $\beta = -0.5$ . Other parameters remain the same as above. In this case, the component represented by  $v = -1$  has a stronger hydrophilicity. We choose circular initial conditions for both  $u$  and  $v$ , as follows:

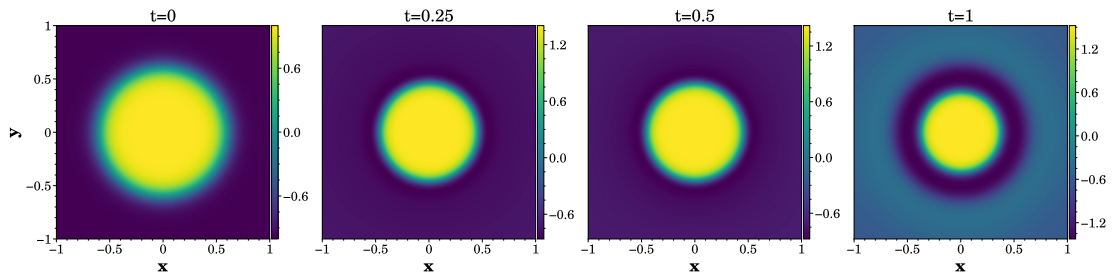
$$\begin{cases} u(x, y; t = 0) = \tanh\left(\frac{0.6 - \sqrt{x^2 + y^2}}{2\varepsilon_u}\right), \\ v(x, y; t = 0) = \tanh\left(\frac{0.6 - \sqrt{x^2 + y^2}}{2\varepsilon_v}\right). \end{cases} \quad (36)$$

Time steps are set as 0.01, 0.04, 0.15, 0.4 and 0.4, with other hyperparameters same as the above experiment. The predicted solutions  $\hat{u}_\theta$  and  $\hat{v}_\theta$  at different time are shown in Fig. 21(a) and Fig. 21(b).

Fig. 21(a) and Fig. 21(b) show the macrophase separation and the microphase separation, respectively. The interior is divided into yellow and dark blue regions, where the dark blue region surrounds the yellow region, similar to the structure of an onion. This indicates that the component represented by the dark blue has a stronger hydrophilicity.



(a) Predicted solutions  $\hat{u}_\theta$  at  $t = 0, 0.25, 0.5, 1$



(b) Predicted solutions  $\hat{v}_\theta$  at  $t = 0, 0.25, 0.5, 1$

**Fig. 21.** Predicted solutions  $\hat{u}_\theta$  and  $\hat{v}_\theta$  obtained by adaptive PINN with time segments lengths of 0.01, 0.04, 0.15, 0.4 and 0.4.

All the above results satisfy the property of mass conservation and the maximum absolute errors are  $O(1)$  and reasonable. From the simulation of these two complex cases, it can be seen that the mass-preserving spatio-temporal adaptive PINN that we have developed can well simulate high-dimensional or complex systems of equations.

#### 4. Conclusion

In this paper, we have introduced the mass-preserving spatio-temporal adaptive PINN that greatly improves the accuracy of PINN for solving high order phase field equations with strong nonlinearity and mass conservation property. Specifically, we add a mass constraint to the loss function and combine it with adaptive sampling methods in space and time.

We conduct several numerical experiments to solve the Cahn-Hilliard equations with Ginzburg-Landau potential and Flory-Huggins potential. This paper provides a detailed description of the process of adjusting the length of time steps based on the rate of energy decrease and modifying their weights according to the mass error. Numerical results show that the modified PINN produces more accurate approximate solutions compared to the baseline PINN with uniform time domain division, while also ensuring mass conservation. Finally, our simulation

results for the three dimensional problem and the system of Cahn-Hilliard equations further indicate the effectiveness and accuracy of the approach. In summary, our modified PINN method is capable of solving high order phase field equations with nonlinearity and singularity.

This method can be applied to solve a broader range of phase field models with mass conservation properties. However, it should be noted that the mass constraint added here is a soft constraint that does not strictly guarantee mass conservation. In future research, we will investigate whether improvements can be introduced to the neural network structure so that the neural network automatically maintains the mass conservation without adding additional constraints, even other physical property of the original model. Thus, a more accurate and efficient machine learning method for solving the phase field equations with with physical property can be obtained.

## References

- [1] J. W. Cahn, J. E. Hilliard, Free energy of a nonuniform system. I. Interfacial free energy, *J. Chem. Phys.* 28 (2) (1958) 258–267.
- [2] J. W. Cahn, On spinodal decomposition, *Acta Metall.* 9 (9) (1961) 795–801.
- [3] D. J. Eyre, Unconditionally gradient stable time marching the Cahn-Hilliard equation, *Mater. Res. Soc. Sympos. Proc.* 529 (1998) 39.
- [4] S. M. Wise, C. Wang, J. S. Lowengrub, An energy-stable and convergent finite-difference scheme for the phase field crystal equation, *SIAM J. Numer. Anal.* 47 (3) (2009) 2269–2288.
- [5] W. Chen, S. Conde, C. Wang, X. Wang, S. M. Wise, A linear energy stable scheme for a thin film model without slope selection, *J. Sci. Comput.* 52 (3) (2012) 546–562.
- [6] H. Gomez, T. J. Hughes, Provably unconditionally stable, second-order time-accurate, mixed variational methods for phase-field models, *J. Comput. Phys.* 230 (13) (2011) 5310–5327.
- [7] F. Guillén-González, G. Tierra, On linear schemes for a Cahn–Hilliard diffuse interface model, *J. Comput. Phys.* 234 (2013) 140–171.
- [8] X. Feng, T. Tang, J. Yang, Stabilized Crank-Nicolson/Adams-Bashforth schemes for phase field models, *East Asian J. Appl. Math.* 3 (1) (2013) 59–80.
- [9] Y. He, Y. Liu, T. Tang, On large time-stepping methods for the Cahn–Hilliard equation, *Numer. Math.* 57 (5-7) (2007) 616–628.

- [10] J. Shen, X. Yang, Numerical approximations of Allen-Cahn and Cahn-Hilliard equations, *Discrete Contin. Dyn. Syst.* 28 (4) (2010) 1669–1691.
- [11] C. Xu, T. Tang, Stability analysis of large time-stepping methods for epitaxial growth models, *SIAM J. Numer. Anal.* 44 (4) (2006) 1759–1779.
- [12] X. Yang, Linear, first and second-order, unconditionally energy stable numerical schemes for the phase field model of homopolymer blends, *J. Comput. Phys.* 327 (2016) 294–316.
- [13] Z. Xu, X. Yang, H. Zhang, Z. Xie, Efficient and linear schemes for anisotropic Cahn–Hilliard model using the stabilized-invariant energy quadratization (S-IEQ) approach, *Comput. Phys. Commun.* 238 (2019) 36–49.
- [14] Q. Pan, C. Chen, Y. J. Zhang, X. Yang, A novel hybrid IGA-EIEQ numerical method for the Allen–Cahn/Cahn–Hilliard equations on complex curved surfaces, *Comput. Meth. Appl. Mech. Eng.* 404 (2023) 115767.
- [15] J. Shen, J. Xu, J. Yang, The scalar auxiliary variable (SAV) approach for gradient flows, *J. Comput. Phys.* 353 (2018) 407–416.
- [16] J. Shen, J. Xu, Convergence and error analysis for the scalar auxiliary variable (SAV) schemes to gradient flows, *SIAM J. Numer. Anal.* 56 (5) (2018) 2895–2912.
- [17] G. Akrivis, B. Li, D. Li, Energy-decaying extrapolated RK–SAV methods for the Allen–Cahn and Cahn–Hilliard equations, *SIAM J. Sci. Comput.* 41 (6) (2019) A3703–A3727.
- [18] Z. Liu, X. Li, The exponential scalar auxiliary variable (E-SAV) approach for phase field models and its explicit computing, *SIAM J. Sci. Comput.* 42 (3) (2020) B630–B655.
- [19] M. Jiang, Z. Zhang, J. Zhao, Improving the accuracy and consistency of the scalar auxiliary variable (SAV) method with relaxation, *J. Comput. Phys.* 456 (2022) 110954.
- [20] L. Ju, J. Zhang, Q. Du, Fast and accurate algorithms for simulating coarsening dynamics of Cahn–Hilliard equations, *Comput. Mater. Sci.* 108 (2015) 272–282.
- [21] X. Li, Convergence analysis of exponential time differencing schemes for the Cahn-Hilliard equation, *Commun. Comput. Phys.* 26 (5) (2019) 1510–1529.

- [22] J. Han, A. Jentzen, W. E, Solving high-dimensional partial differential equations using deep learning, *Proc. Natl. Acad. Sci. U. S. A.* 115 (34) (2018) 8505–8510.
- [23] J. Han, A. Jentzen, W. E, Deep learning-based numerical methods for high-dimensional parabolic partial differential equations and backward stochastic differential equations, *Commun. Math. Stat.* 5 (4) (2017) 349–380.
- [24] M. Raissi, P. Perdikaris, G. E. Karniadakis, Physics-informed neural networks: A deep learning framework for solving forward and inverse problems involving nonlinear partial differential equations, *J. Comput. Phys.* 378 (2019) 686–707.
- [25] Y. Gu, H. Yang, C. Zhou, Selectnet: Self-paced learning for high-dimensional partial differential equations, *J. Comput. Phys.* 441 (2021) 110444.
- [26] A. D. Jagtap, G. E. Karniadakis, Extended physics-informed neural networks (xpinns): A generalized space-time domain decomposition based deep learning framework for nonlinear partial differential equations, *Commun. Comput. Phys.* 28 (5) (2020).
- [27] R. Matthey, S. Ghosh, A novel sequential method to train physics informed neural networks for Allen-Cahn and Cahn-Hilliard equations, *Comput. Meth. Appl. Mech. Eng.* 390 (2022) 114474.
- [28] K. Tang, X. Wan, C. Yang, Das-pinns: A deep adaptive sampling method for solving high-dimensional partial differential equations, *J. Comput. Phys.* 476 (2023) 111868.
- [29] Z. Gao, L. Yan, T. Zhou, Failure-informed adaptive sampling for PINNs, *SIAM J. Sci. Comput.* 45 (4) (2023) A1971–A1994.
- [30] J. Guo, H. Wang, C. Hou, A novel adaptive causal sampling method for physics-informed neural networks, *arXiv preprint arXiv:2210.12914* (2022).
- [31] C. Wu, M. Zhu, Q. Tan, Y. Kartha, L. Lu, A comprehensive study of non-adaptive and residual-based adaptive sampling for physics-informed neural networks, *Comput. Meth. Appl. Mech. Eng.* 403 (2023) 115671.
- [32] L. Lu, X. Meng, Z. Mao, G. E. Karniadakis, Deepxde: A deep learning library for solving differential equations, *SIAM Rev.* 63 (1) (2021) 208–228.
- [33] C. L. W. Zhao, et al., Solving Allen-Cahn and Cahn-Hilliard equations using the adaptive physics informed neural networks, *Commun. Comput. Phys.* 29 (3) (2021) 930–954.

- [34] X. Meng, Z. Li, D. Zhang, G. E. Karniadakis, PPINN: Parareal physics-informed neural network for time-dependent PDEs, *Comput. Meth. Appl. Mech. Eng.* 370 (2020) 113250.
- [35] S. Wang, Y. Teng, P. Perdikaris, Understanding and mitigating gradient flow pathologies in physics-informed neural networks, *SIAM J. Sci. Comput.* 43 (5) (2021) A3055–A3081.
- [36] Z. Xiang, W. Peng, X. Liu, W. Yao, Self-adaptive loss balanced physics-informed neural networks, *Neurocomputing* 496 (2022) 11–34.
- [37] S. Lin, Y. Chen, A two-stage physics-informed neural network method based on conserved quantities and applications in localized wave solutions, *J. Comput. Phys.* 457 (2022) 111053.
- [38] S. Theodoridis, Stochastic gradient descent, *Mach. Learn.* (2015) 161–231.
- [39] D. P. Kingma, J. Ba, Adam: A method for stochastic optimization, *arXiv preprint arXiv:1412.6980* (2014).
- [40] D. C. Liu, J. Nocedal, On the limited memory BFGS method for large scale optimization, *Math. Program.* 45 (1) (1989) 503–528.
- [41] M. I. M. Copetti, C. M. Elliott, Numerical analysis of the Cahn-Hilliard equation with a logarithmic free energy, *Numer. Math.* 63 (1992) 39–65.
- [42] C. M. Elliott, H. Garcke, On the Cahn–Hilliard equation with degenerate mobility, *SIAM J. Math. Anal.* 27 (2) (1996) 404–423.
- [43] C. Liu, J. Shen, A phase field model for the mixture of two incompressible fluids and its approximation by a Fourier-spectral method, *Phys. D* 179 (3-4) (2003) 211–228.
- [44] Y. Hirai, E. Avalos, T. Teramoto, Y. Nishiura, H. Yabu, Ashura particles: Experimental and theoretical approaches for creating phase-separated structures of ternary blended polymers in three-dimensionally confined spaces, *ACS Omega* 4 (8) (2019) 13106–13113.
- [45] G. Ji, Z. Xu, Y. Yang, An efficient and unconditionally energy stable fully discrete scheme for the confined ternary blended polymers model, *CSIAM Trans. Appl. Math.* 3 (3) (2022) 480–514.
- [46] E. Avalos, T. Higuchi, T. Teramoto, H. Yabu, Y. Nishiura, Frustrated phases under three-dimensional confinement simulated by a set of coupled cahn–hilliard equations, *Soft matter* 12 (27) (2016) 5905–5914.